Aerodynamic and Aeroacoustic Performance of Airfoils Fitted with Morphed trailing edges

Hasan Kamliya Jawahar*, Mahdi Azarpeyvand†
University of Bristol, Bristol, United Kingdom, BS8 1TR
and
Carlos R. Ilário da Silva‡
Embraer, São José dos Campos, 12227-901, Brazil

Experimental and numerical studies of a simple NACA 0012 airfoil fitted with two different flap profiles were successfully carried out to characterize their aerodynamic and aeroacoustic performance. The airfoil was tested with two flap configurations with different flap camber and a flap deflection angle of $\beta = 10°$. The aerodynamic lift and drag measurements show improved lift-to-drag performance for the morphed flap airfoil. Surface flow visualization has shown delayed separation for the morphed flap airfoil. Flow measurements showed that the downstream wake development can be significantly influenced by the flap profile. Particle Image Velocimetry was used to study the flow over the flap and airfoil wake. The tests were carried out for a flow velocity of $U_\infty = 20$ m/s, corresponding to a chord-based $Re_c = 2.6 \times 10^5$. The mean velocity contours at the wake showed increased wake deficit and turbulent kinetic energy for the morphed flap airfoil compared to the hinged flap airfoil. The turbulent kinetic energy results displayed a characteristic double peak behavior which was also the dominant content of the streamwise normal Reynolds shear stress component. Large eddy simulations were carried out for the two airfoils and the results were validated with the experimental measurements. The boundary layer profile from the computations showed delayed separation. The wall pressure spectra close to the trailing edge showed increased energy for the morphed flap airfoil relative to the hinged flap airfoil. The Curle's acoustic analogy was used to calculate the far-field noise measurements and morphed flap airfoil showed increased noised compared to the hinged flap airfoil.

Nomenclature

b	=	trailing edge flap length, m
c	=	airfoil chord length, m
C_L	=	lift coefficient
C_D	=	drag coefficient
l	=	airfoil span length, m
$L_x \times L_y \times L_z$	=	cell dimensions of computational grid
M	=	Mach number
p_{ref}	=	reference pressure ($= 2 \times 10^{-5}$), Pa
Q	=	second invariant of the velocity-gradient tensor, $1/s^2$
Re_c	=	chord-based Reynolds number
S	=	wing area, m^2
U, U_∞	=	mean velocity, free-stream velocity, m/s
$\overline{u'u'}$	=	streamwise Reynolds normal stress component
$\overline{v'v'}$	=	crosswise Reynolds normal stress component
$\overline{u'v'}$	=	Reynolds shear stress component
x, y, z	=	streamwise, crosswise and spanwise coordinates, m
y^+	=	dimensionless wall distance
α	=	angle of attack, °
β	=	morphing flap tip deflection angle, °
Φ_{pp}	=	wall-pressure power spectral density, Pa^2/Hz

*PhD Student, Department of Aerospace Engineering, AIAA Student Member, hasan.kj@bristol.ac.uk
†Reader in Aeroacoustics, Department of Mechanical Engineering, m.azarpeyvand@bristol.ac.uk
‡Technology Development Engineer, Embraer, Sáo José dos Campos, Brazil, carlos.ilario@embraer.com.br

I. Introduction

SHAPE-ADAPTIVE structures are enabling wind turbine blades and aeroplane wings of improved performance with reduced weight and complexity penalty. Containing smooth geometric changes and continuous structural surfaces, these compliant light-weight control surfaces, which are increasingly known as morphing structures, remain conformal to the flow. As such, significant noise and drag reduction are envisaged through morphing structures. It is of fundamental importance in the concept synthesis of morphing structures to thoroughly investigate the flow behaviours and mechanisms of performance improvement.

Studies have shown that noise generated by kinetic energy scattering of turbulent eddies in the boundary layer as they cross the wing's trailing edge becomes dominant for aeroplanes in clean configuration with projected reduction of the high-lift system noise [1]. As such, airfoil self-noise has been considered as an important component of airframe noise during take-off and landing. Some of the currently employed passive methods for airfoil trailing edge noise reduction includes serrated trailing edges [3, 4], porous surface treatments [5–8] and morphing trailing edges [9–12]. With the use of morphing surfaces our aim is to address transition delay, separation postponement, lift enhancement, drag reduction, turbulence augmentation and noise suppression [13]. An ideal method of morphing should achieve the control goal without affecting other goals adversely. However, in reality, continuous compromises and trade-offs have to be made for a particular design goal as it is almost impossible to decouple the interlinked flow behaviour [13], *i.e.* lift and drag forces and noise emission in the case of the high-lift systems.

Several studies of morphing structures have shown the smooth curvature has significant effects on aerodynamic performance of airfoils. Most of the studies showed much interest on than the morphing structures and mechanism [14–20] than the aerodynamic and aeroacoustic performance. An innovative trailing-edge morphing mechanism that uses a honeycomb core with axial variable stiffness developed by Ai *et al.* [19, 20], was used as morphing profile for the experimental and computational studies carried out by Jawahar *et al.* [10–12]. The recent study Jawahar *et al.* [12] showed that small changes in the flap camber profile of the morphed flap can change the aerodynamic behaviour significantly. The lift and drag were shown to be affected with flap with higher camber producing larger lift but with higher drag. The boundary layer behaviour showed delayed separation for the morphed flap airfoil relative to the conventional hinged flap configuration. The turbulence levels at the wake were also found to be significantly altered with the morphed flap having higher magnitude. This study concluded that independent surface morphing would aid in the favourable delayed separation while reducing the unfavourable increased drag.

Complimenting the previous study [12] the current experimental and numerical study investigates aerodynamic and aeroacoustic behavior for a morphed and hinged airfoil with a trip. This paper presents a detailed aerodynamic study with lift and drag measurements, surface flow visualization, Particle Image Velocimetry. Further high fidelity Large Eddy Simulations were carried out and the results for the boundary layer measurements, wake flow structure, unsteady surface pressure, coherence and far-field noise measurements were presented.

II. Wind Tunnel and Experimental Setup

NACA 0012 airfoil fitted with two different flaps have been experimentally tested at the low turbulence closed-circuit wind tunnel facility at the University of Bristol. The wind tunnel has an octagonal working section of 0.8 m × 0.6 m × 1 m, contraction ratio of 12:1, a maximum velocity of 100 m/s and operates with turbulence levels as low as 0.05% [21]. The tested NACA 0012 airfoil has a chord length of $c = 0.2$ m and a span length of $l = 0.45$ m. The boundary layer was tripped at $0.1c$ (see Fig. 1a) on both the sides of the airfoil with a serrated turbulator tape having a height of 0.5 mm and serration angle of 60° [22, 23]. The tests were carried out at a freestream velocity of $U_\infty = 20$ m/s corresponding to a chord-based Reynolds number of $Re_c = 2.6 \times 10^5$ at Mach number $M \approx 0.058$. Two circular side-plates with a radius of 0.17 m were used to reduce the three-dimensionality effects of the flow around the airfoil. The airfoil was designed such that it facilitates installation of two interchangeable trailing edge flaps with a length of $b = 0.06$ m ($0.3c$) and a deflection angle of, $\beta = 10°$ (see Fig. 1b). Ai *et al.* [19, 20] tested the aerodynamic and aeroacoustic performance of novel morphed flaps using Xfoil-BPM model. The results from these studies were then used to design the morphed flap camber profiles and further experimental and computational studies [10–12] were carried out. In the current study, NACA 0012 airfoil with morphed flap profiles (see Fig. 1b) having the lowest C_L (Hinged Flap, HF) and highest C_L (Morphed Flap, MF) from the previous studies [10–12] were used to further understand the aerodynamic, aeroacoustic and wake turbulence characteristics of the airfoils fitted with morphed flap.

To study the flow pattern over the morphed trailing edge oil-flow visualization tests were carried out. The airfoil was covered with matt black vinyl sheet to visualize the flow better. A mixture of paraffin and oleic acid in a ratio of 20:1 along with the white pigmenting agent titanium dioxide was used in the present study. In order to effectively capture the boundary layer behavior, the consistency of the oil mixture was tested in order to have the inertial forces of the oil mixture lower than viscous and surface tension forces [24, 25].

The aerodynamic lift and drag force measurements were carried out using an AMTI OR6-7-2000 force platform from Advanced Mechanical Technology Inc., mounted at the base of the set-up. The data were collected for a period of 16 s with a sampling frequency of 2000 Hz, which deemed sufficient enough based on an uncertainty analysis of the collected data.

The flow behavior around the airfoil and in the wake region was captured using Particle Image Velocimetry (PIV). The PIV measurements were carried out using a Dantec DualPower 200 mJ Nd:YAG laser with a width of 1 mm and wavelength of 532 nm placed mid-span of the airfoil. The laser sheet was set to have a time interval of 18 μs between each pulse and a repetition rate of 2.5 Hz. A mixture of Polyethylene glycol 80 with a mean diameter of 1 μm was used to seed the air inside the low turbulence wind tunnel. A total number of 2400 images for each measurement were captured using a FlowSense 4 MP CCD camera with a resolution of 2078 $\times$ 2078 pixels and 14 bit, corresponding to field view of 9.5 cm $\times$ 9.5 cm. As shown in Fig. 2, a total of three measurement windows of the same size were used for every tested angle of attack. A matt black vinyl sheet was used to cover the airfoil to reduce the laser reflection from the airfoil's surface. The PIV images were analyzed with the DynamicStudio software from Dantec. The tests were performed for angles of attack, $\alpha = 0°, 2°, 4°, 6°$ and $8°$ at the freestream velocity of $U_\infty = 20$ m/s, corresponding to chord-based Reynolds number of $Re_c = 2.6 \times 10^5$.

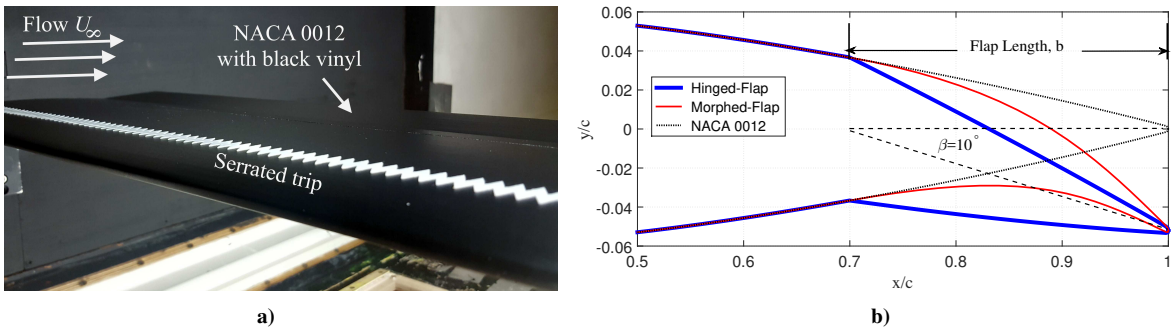

a) b)

Fig. 1. a) NACA 0012 airfoil set up in the low-turbulence wind tunnel and b) Geometric details of the NACA 0012 airfoil with a trailing edge deflection angle of $\beta = 10°$ characterised into Hinged Flap and Morphed Flap airfoils.

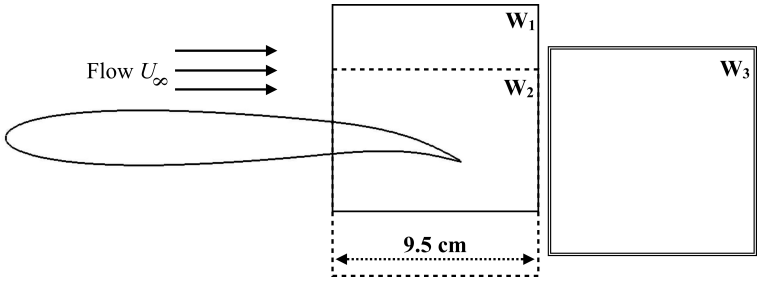

Fig. 2. Camera window locations used for the PIV measurements.

III. Computational Setup

Large Eddy Simulations (LES) based on spatially filtered, incompressible Navier-Strokes equations with the dynamic Smagorinsky subgrid scale model [26] was carried out to further investigate the airfoil flow characteristics. Previous RANS and DES studies [10,11] were carried out to understand the aerodynamic and aeroacoustic characteristics of the airfoil with morphed trailing edges. However, the aeroacoustic results showed narrowband peaks that developed due to the boundary layer instabilities. Therefore in order to eliminate them, a boundary layer step-trip was employed in the current study. A step-trip with a height of 8 mm ($0.04c$) and a length of 3 mm ($0.015c$) was placed at the location $0.1c$ downstream the leading edge on both the sides of the airfoil. A three-dimensional multi-block structured C-H type mesh with a domain size of $10c$ in the streamwise, $5c$ in the crosswise direction and $0.1c$ spanwise thickness [27–30] was used. The step-trip airfoils had a cell distribution of $L_x \times L_y \times L_z = 704 \times 40 \times 64$ at regions close to the airfoil with the 40 grid points within $y = 0.035c$ close to the wall resulting in a $y^+ \approx 0.5 - 1$. The far-field region around the airfoil had a cell distribution of $L_x \times L_y \times L_z = 352 \times 150 \times 32$. The grid spacing along the streamwise direction corresponds

to $x^+ \approx 15$ and is clustered toward the airfoil leading-edge and trailing edge. An area of $1.5c$ downstream of the trailing edge was densely populated with 400 grid points in the streamwise direction to capture the wake behavior accurately. In the spanwise direction, the grid spacing was uniformly distributed corresponding to $z^+ \approx 20$. The final computational mesh had 11.5 million cells in total. A close-up view of the airfoil trailing edge mesh is shown in Fig. 3. All the simulations were carried out for 30 flow through times (FTT) and the data were collected for only the last 10 FTT. A CFL value of $C_{max} \leq 1$ was maintained throughout the simulations with a time-step of $\Delta t = 2.2 \times 10^{-6}$ s.

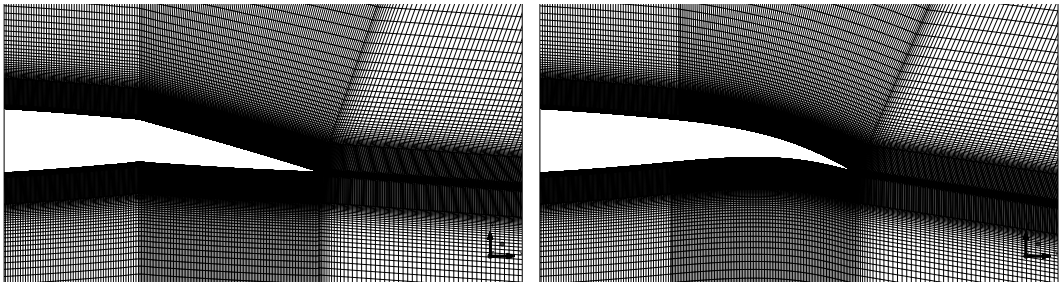

a) Hinged Flap **b) Morphed Flap**

Fig. 3. Grid refinement close to the airfoil wall and the wake regions to capture the boundary layer transition over the flaps accurately.

IV. Results and Discussion

A. Aerodynamic Force Measurements

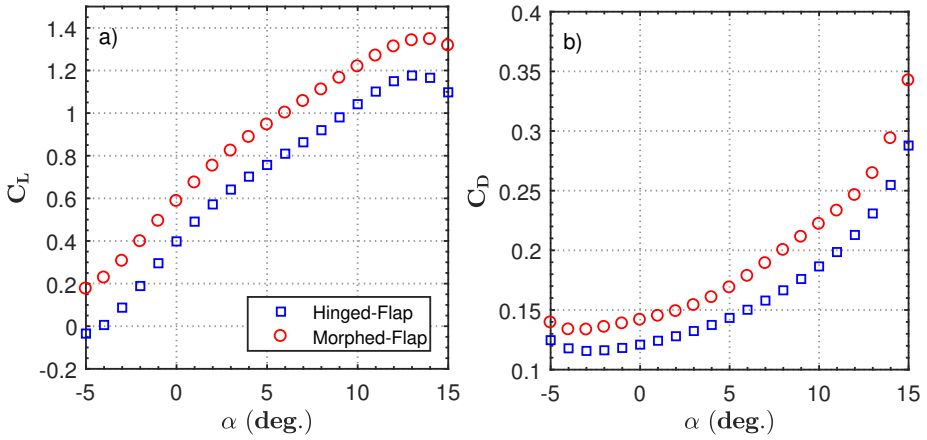

Fig. 4. Lift and drag coefficient results for the Hinged Flap and Morphed Flap airfoil at a freestream velocity of $U_\infty = 20$ m/s ($Re_c = 2.6 \times 10^5$).

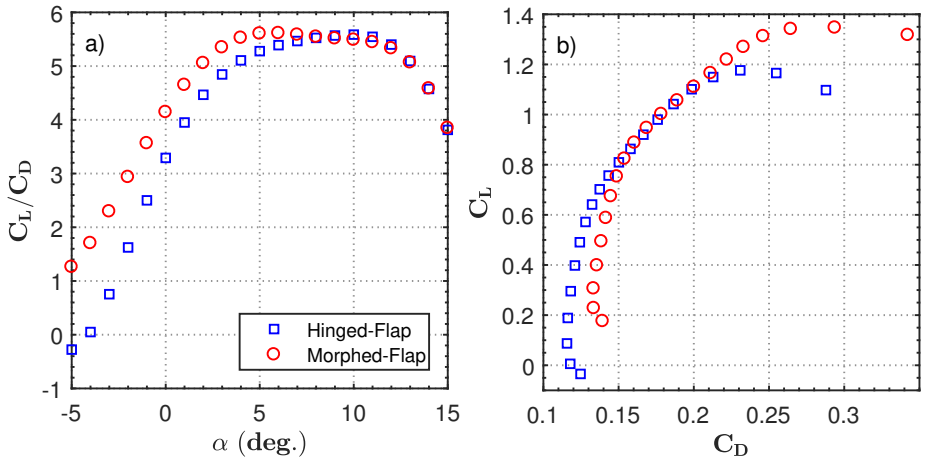

Fig. 5. Lift-to-drag coefficient ratio results and the drag polar plots for the Hinged Flap and Morphed Flap airfoil at a freestream velocity of $U_\infty = 20$ m/s ($Re_c = 2.6 \times 10^5$).

The results of the aerodynamic force measurements for NACA 0012 airfoil fitted with the Hinged Flap (HF) and Morphed Flap (MF) having a deflection angle of $\beta = 10°$ is presented in Fig. 4. A serrated turbulator tape has been used on both the sides of the airfoil surface to make the boundary layer flow turbulent. The tests were carried out for angles of attack ranging from $\alpha = -5°$ to 15°. The results of the lift coefficients $C_L - \alpha$ presented in Fig. 4a show a better overall lift performance for the MF airfoil compared to the HF airfoil. The C_L-α curve of the MF airfoil has an average lift increment of $\Delta C_L = 0.191$ compared to the HF airfoil over the tested angles of attack. The largest difference in the lift coefficient between the HF and MF airfoil $\Delta C_L = 0.222$ was produced at $\alpha = -5°$ and the lowest $\Delta C_L = 0.165$ was produced at the stall angle of attack $\alpha = 13°$, which corresponds to a 14% increase in the lift coefficient for the MF airfoil relative to the HF airfoil at $C_{L,max}$. The MF airfoil reduces the angle of attack for a given lift coefficient by $\alpha = 3°$ compared to the HF airfoil. The stall angle of both the airfoils remains unchanged, which is consistent with the results in the literature [31]. The drag coefficient results $C_D - \alpha$ presented in Fig. 4b show a generic airfoil $C_D - \alpha$ trend with lower values of C_D at low angles of attack and increasing values of C_D as the angle of attack is increased. The difference in drag coefficient between the HF and MF airfoil was found to be $\Delta C_D = 0.0148$ at the angle of attack $\alpha = -5°$ with the MF airfoil having larger drag coefficient relative to the HF airfoil. The largest difference in drag coefficient $\Delta C_D = 0.0545$ was found at the post-stall angle of attack $\alpha = 15°$ with the MF airfoil producing higher C_D values. In the pre-stall regions, the largest $\Delta C_D = 0.0148$ was found at the stall angle of attack $\alpha = 13°$.

The lift-to-drag coefficient ratio results and the drag polar curves for both the HF and MF airfoils are presented in Fig. 5. The results for the lift-to-drag coefficient ratio are presented in the Fig. 5a. The results show a large difference in the lift-to-drag coefficient ratio between the HF and MF airfoil at low angles of attack and this difference in performance between the airfoils decrease as the angle of attack is increased. The MF airfoil has an overall superior aerodynamic lift performance compared to the HF airfoil. There is no or insignificant difference in the C_L/C_D performance between the airfoils for angles of attack larger than $\alpha > 7°$. The largest difference in the lift-to-drag coefficient ratio of $\Delta(C_L/C_D) = 0.984$ was found between the HF and MF airfoil at the angle of attack $\alpha = -5°$ with the MF airfoil portraying better performance with larger values of C_L/C_D. As the angle of attack is increased to $\alpha = 0°$ and $5°$ the differences in the $\Delta(C_L/C_D)$ value reduces to 0.852 and 0.328 respectively, which corresponds to an increased performance of up to 26% and 6% for the MF airfoil relative to the HF airfoil. The largest value of $C_L/C_D = 5.60$ was achieved by MF airfoil at $\alpha = 5°$. The results for the drag polar curves are presented in the right side of the Fig.5b. As mentioned earlier, the MF airfoil reduces the angle of attack for a given lift coefficient by $\alpha = 3°$. The drag polar plot shows that the MF airfoil produces slightly higher lift and a lower drag at $\alpha = 10°$ compared to the $\alpha = 13°$ of the HF airfoil.

B. Surface Flow Visualization

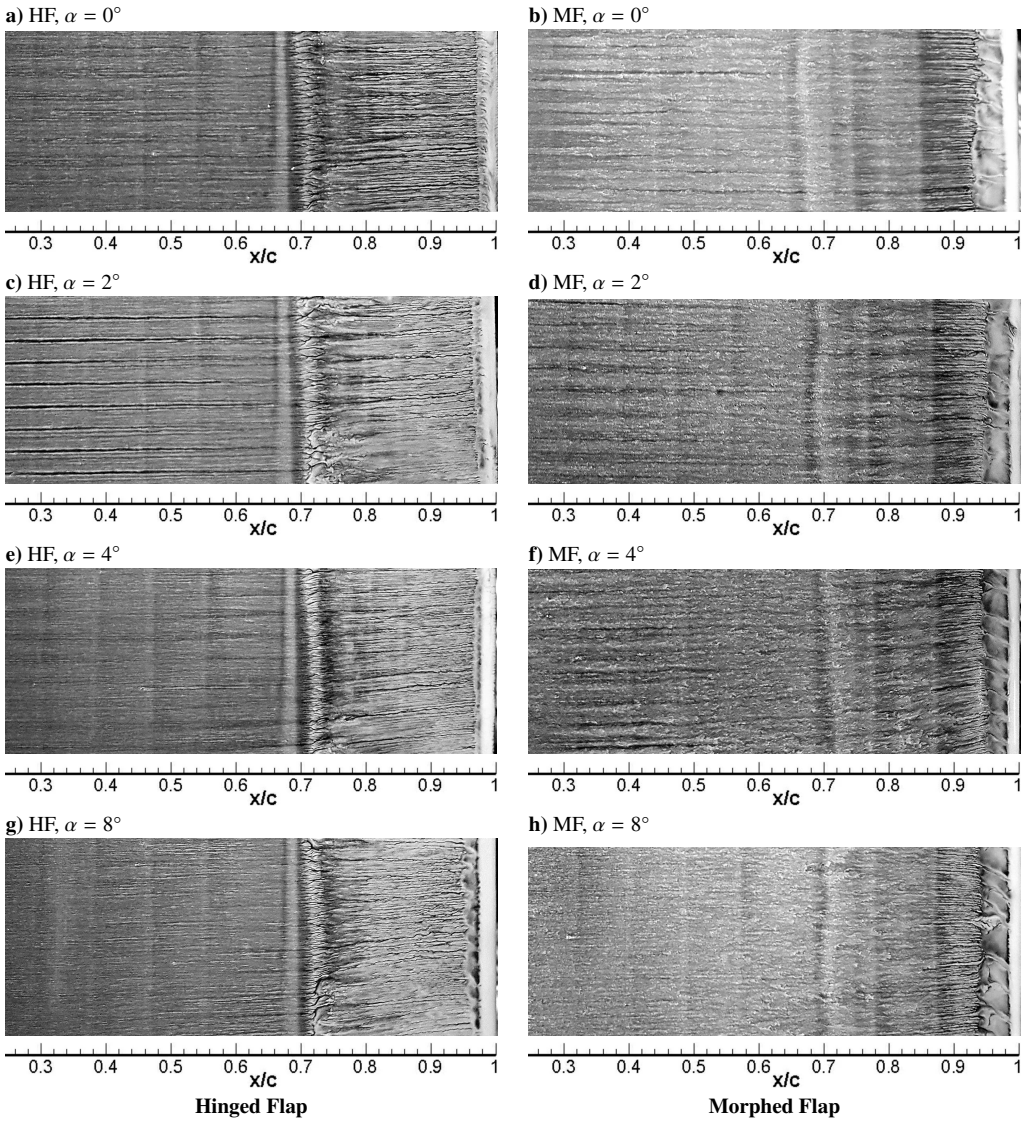

Fig. 6. The photographs of the oil-flow visualization patterns over the suction side of the Hinged Flap and Morphed Flap airfoil at the vicinity of the flap tested at a freestream velocity of $U_\infty = 20$ m/s ($Re_c = 2.6 \times 10^5$).

The oil-flow visualization technique was used on both the suction and pressure sides of the airfoil to visualize the boundary layer behavior and flow separation point on the airfoil flap surfaces. The tests were carried out for angles of attack ranging from $\alpha = -4°$ to 16° in increments of 2°. However, for the purpose of brevity, the results are presented only for the suction side of the airfoil at angles of attack $\alpha = 0°, 2°, 4°$ and 8° in Fig. 6. The photographs of the oil-flow visualization presented in Fig. 6 show the results of the HF airfoil in the left column and the MF airfoil results in the right column with the different rows showing different angles of attack. At the first glance, the results clearly show that for the HF configuration the boundary layer flow on the suction side of the airfoil separates at the hinge point of the flap at $x/c = 0.7$ for all the presented angles of attack. For the MF airfoil, the flow does not separate over the flap until $x/c = 0.95$ for angles of attack $\alpha = 0°$ and 2°. As the angle of attack is increased the separation point on the flap for the MF airfoil moves upstream to locations $x/c = 0.8$ and $x/c = 0.75$ for angles of attack $\alpha = 4°$ and 8°, respectively. Even though the test results are also available for the pressure side it is not presented due to the absence of any unique flow feature or separation on the airfoil flap surfaces for the entire range of tested angles of attack. It is also noteworthy that turbulent wedges that formed the of downstream of the serrated turbulator present at $0.1c$ were also observeed in previous flow visualization studies [22, 23]. Smaller regions of recirculation were found in-between the serration wedges which may have served to trip the flow and lead to the formation of the turbulent wedges. These are seen as horizontal lines seen in the photographs in Fig. 6. The vertical lines seen in Fig. 6 are the shade arising due to the pressure taps that lay below the black vinyl used to cover the airfoil.

C. Flow Visualization

The results of the mean velocity contours at the HF and MF airfoil flap and wake region, measured using PIV technique are presented in Fig. 7. The tests were carried out at a freestream velocity of $U_\infty = 20$ m/s and the results are presented for angles of attack $\alpha = 0°$, 2°, 4° and 8°. In Fig. 7 the results for the MF airfoil are presented in the left column and the results for the HF airfoil are presented in the right column. The normalized streamwise velocity results presented in Fig. 7a, 7b, 7c and 7d show that for angles of attack $\alpha = 0°$ and 2°, the flow separates at the hinge location $x/c = 0.7$ for the HF airfoil but remains close to the wall, whereas for the MF airfoil the flow separates only at $x/c = 0.95$. The results for the MF airfoil show negative velocity close to the trailing edge indicating a separation bubble, which is absent in the case of the HF airfoil. For the angle of attack, $\alpha = 4°$ shown in Fig. 7e and 7f, the flow separates at the hinge point $x/c = 0.7$ for the HF airfoil whereas, the flow separates only at $x/c = 0.9$ for the MF airfoil. As the angle of attack is increased to $\alpha = 8°$ for the HF airfoil the separation point remains unchanged but for the MF airfoil, the separation point moves upstream to $x/c = 0.85$. The separation bubble close to the trailing edge of the MF airfoil at $\alpha = 8°$ is substantially larger compared to the HF airfoil.

The normal components of the Reynolds stress tensors ($\overline{u'u'}, \overline{v'v'}$) are presented in Figs. 8 and 9 respectively, over the flap and wake region of the HF and MF airfoils. The same color scales are used for each angle of attack to facilitate comparison of the plots for the presented results. The boundary layer separation locations over the flap region discussed above for both the HF and MF airfoil can be seen much more distinctively in the Reynolds stress tensor plots presented in Figs. 8 and 9. The results of the streamwise normal Reynolds stress components ($\overline{u'u'}$) in Fig. 8 clearly shows two distinct regions of high $\overline{u'u'}$ values found at the wake location for both the HF and MF airfoil at all the presented angles of attack. For the angles of attack, $\alpha = 0°$ and 2° high values of $\overline{u'u'}$ are found on both the upper and lower side of the wake. The stresses on the wake upper side decay quicker compared to the wake lower side at further downstream locations for both the airfoils. The MF airfoil has higher values of $\overline{u'u'}$ on the upper side relative to the HF airfoil for these two angles of attack. For the angles of attack $\alpha = 4°$ and $\alpha = 8°$, the values of $\overline{u'u'}$ are wider compared to the previously discussed lower angles of attack. The early separation at these angles of attack gives rise to higher values of $\overline{u'u'}$ over the flap surfaces for both the airfoils. The lower side of the MF airfoil at $\alpha = 8°$ has the highest values of $\overline{u'u'}$ compared to HF airfoil. These high values for the MF airfoil are due to the tip of the trailing edge interfering with the flow at a higher angle relative to the trailing edge of the HF airfoil. The contours of the crosswise normal Reynolds stress component $\overline{v'v'}$ in Fig. 9 regions of increased magnitude closer to the trailing edge. The MF airfoil produces higher values of $\overline{v'v'}$ closer to the trailing edge relative to the HF airfoil for all the presented angles of attack.

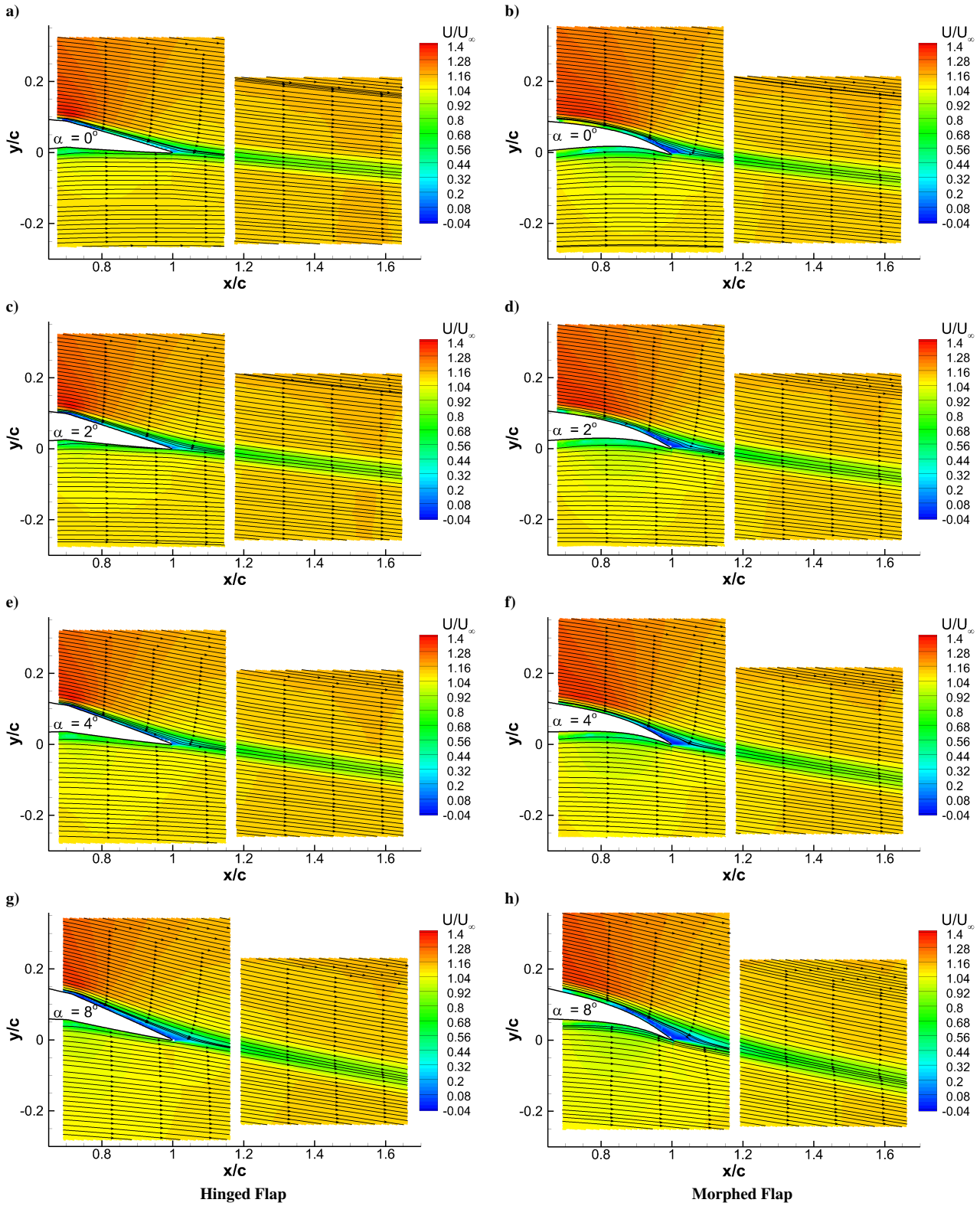

Fig. 7. Mean velocity contours from PIV for the Hinged Flap and Morphed Flap airfoils.

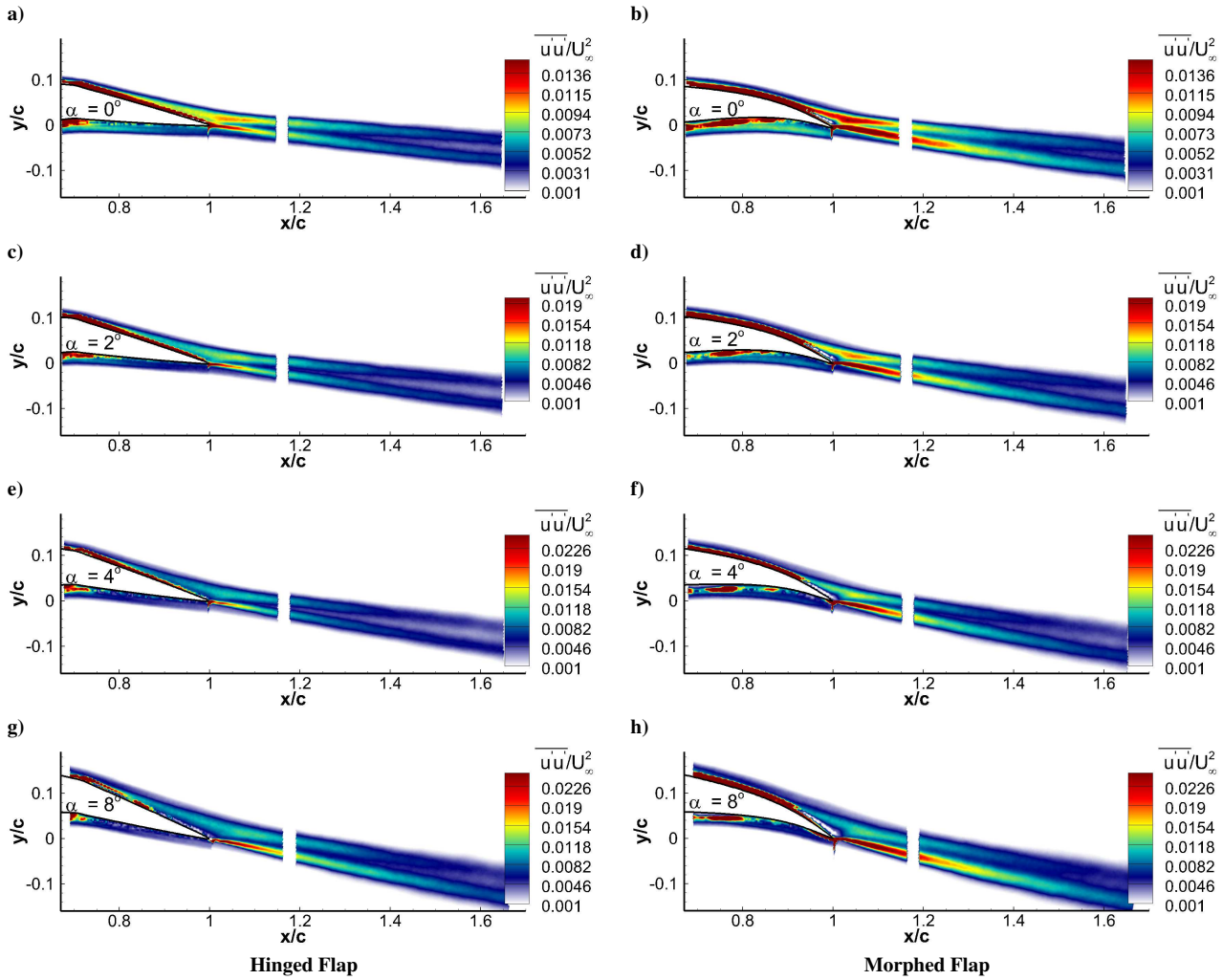

Fig. 8. Streamwise normal Reynolds stress contours for the Hinged Flap and Morphed Flap airfoils.

D. Wake Development

The wake flow field of both the HF and MF airfoil was studied experimentally using PIV technique. Detailed line plots from the PIV has been presented for six downstream locations in the mid-span position of the airfoil, x/c = 1.025, 1.05, 1.10, 1.20, 1.40 and 1.60 with the leading-edge tip assumed as the datum point as shown in Fig. 11. The tests were performed for angles of attack, $\alpha = 0°, 2°, 4°, 6°$ and 8° at the freestream velocity of U_∞ = 20 m/s, corresponding to $Re_c = 2.6 \times 10^5$.

The mean velocity profiles for angles of attack $\alpha = 0°, 2°, 4°$ and 8° are presented in Figs. 12. The velocity profiles for all the presented angles of attack at the near-wake location x/c = 1.025 show an increased velocity deficit for the MF airfoil relative to the HF airfoil. At further downstream locations x/c = 1.20, 1.40 and 1.60, the overall results for all the presented angles of attack show that the wake velocity for the MF airfoil has an increased deflection angle compared to the HF airfoil. The MF airfoil has increased velocity deficit relative to the HF airfoil at all the downstream wake locations.

The non-dimensional turbulent kinetic energy (TKE) results from the PIV measurements for the HF and MF airfoils at angles of attack $\alpha = 0°, 2°, 4°$ and 8° are presented in Fig. 13. The TKE magnitude results clearly show the characteristic double peak wake behavior close to the trailing edge, which arises due to the boundary layers from the upper and lower side. For all the presented angles of attack, at the near-wake location, x/c = 1.025 and x/c = 1.05 close to the trailing edge, it can be observed that the peak for the MF airfoil is higher peak magnitude toward the pressure side. This is due to the interference of the MF airfoil trailing edge with the freestream flow. The TKE magnitude for the HF airfoil is about 50% lower relative to the MF airfoil at this peak regions. The TKE magnitude peak for the HF airfoils is up to 20% lower at the locations x/c = 1.10 and x/c = 1.20 relative to the MF airfoil. This

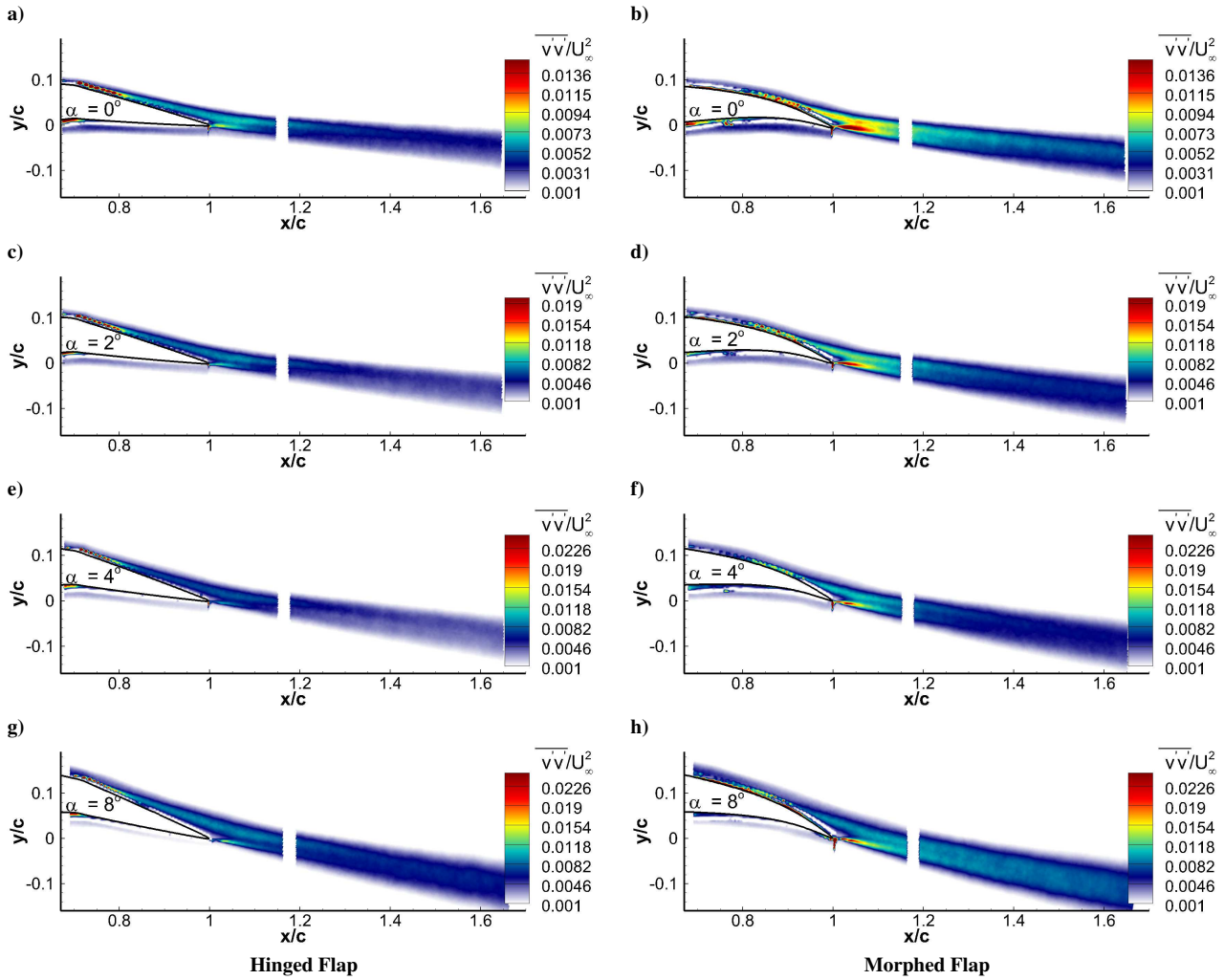

Fig. 9. Crosswise normal Reynolds stress contours for the Hinged Flap and Morphed Flap airfoils.

difference in the TKE magnitude between the two airfoils reduces at further downstream locations. At the far-wake locations, $x/c = 1.20$, 1.40 and 1.60, it can be observed that the MF airfoil has a wider wake towards the pressure surface than that of HF airfoil.The Reynolds shear stress components ($\overline{u'v'}$) are presented in Figs. 10 and 14. The shear stress $\overline{u'v'}$ for the MF airfoil is larger than that of the HF airfoil at the near-wake locations $x/c = 1.025$, $x/c = 1.05$ and $x/c = 1.10$ for all the presented angles of attack. However, the stresses at far-wake downstream locations are similar between the two cases for all the presented angles of attack but with the MF airfoil having wider shear relative to the HF airfoil due to the angle of the trailing edge tip to the freestream flow.

The aerodynamic behavior seen in the previous sections shows increased C_L/C_D for the MF airfoil compared to the HF airfoil. The surface flow and the wake flow behavior show us that the MF airfoil has delayed separation and increased turning angle. This increased turning angle aids in the increased lift seen before and the longer region of attached flow near the trailing edge of the MF airfoil aids in the reduction of form drag. This hypothesis is also supported by the flow behavior seen previously in the Gurney flap studies [32, 33].

E. Computational Fluid Dynamics

In addition to the experimental measurements and the discussions presented in the above sections, detailed LES studies using dynamic Smagorinsky were carried out for selected angles of attack of $\alpha = 0°$ and $\alpha = 4°$ for both the HF and MF airfoils. The following results will aid us to better understand the flow structures and aeroacoustic behavior of the morphed airfoils. The wake velocity results from the experiments were used to validate the results from the simulations.

The mean velocity results from the LES simulations are compared with the experimental measurements at the wake

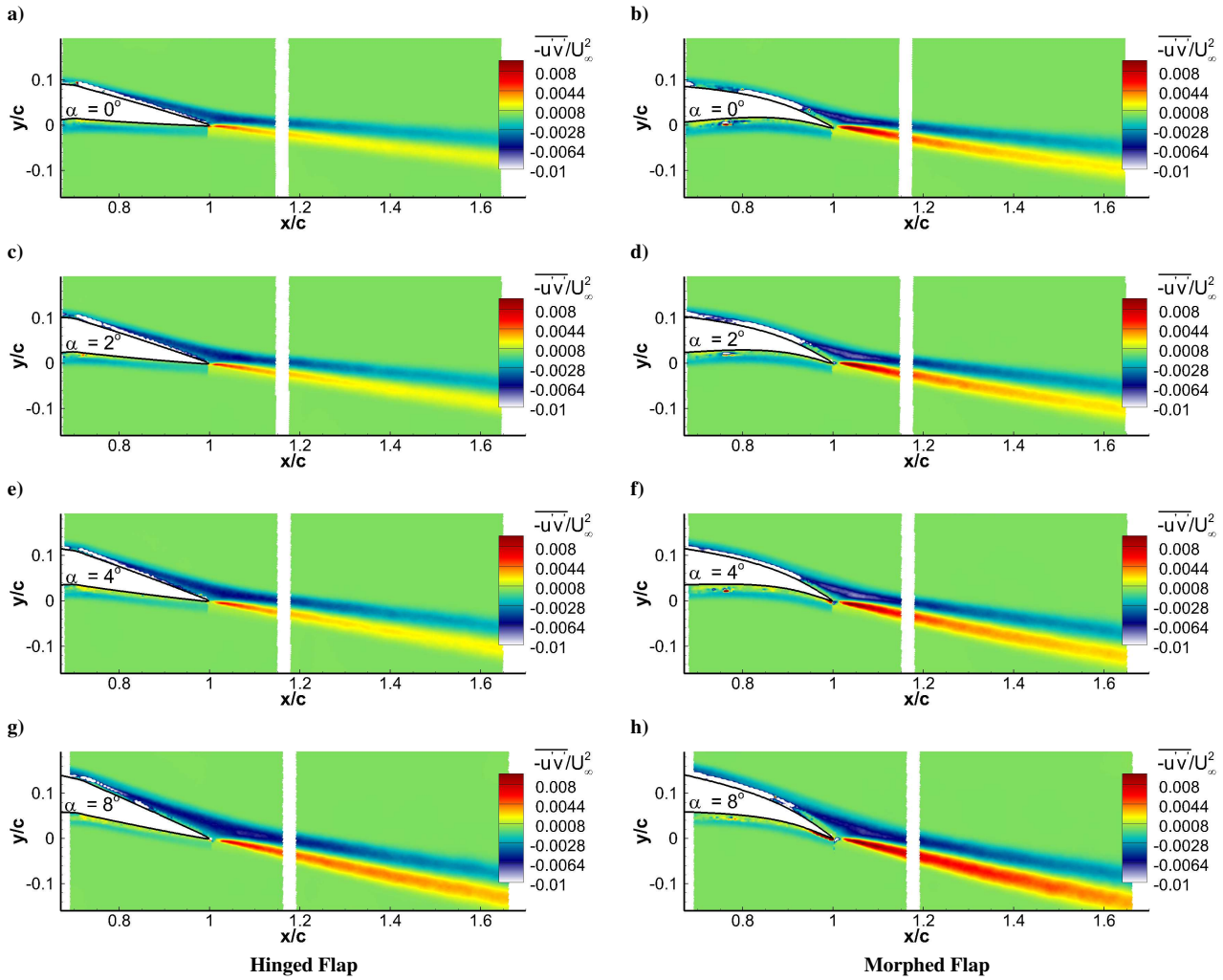

Fig. 10. Reynolds shear stress contours for the Hinged Flap and Morphed Flap airfoils at a freestream velocity of $U_\infty = 20$ m/s ($Re_c = 2.6 \times 10^5$).

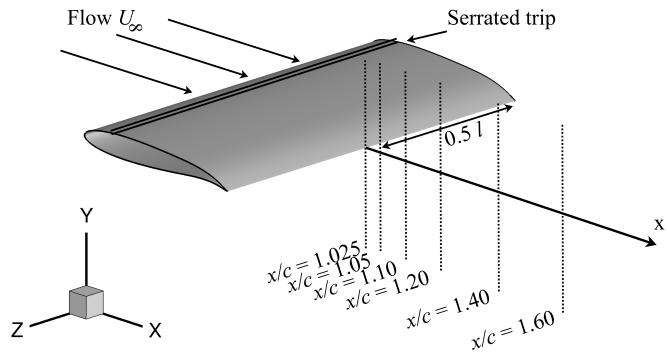

Fig. 11. Airfoil coordinate system along with wake velocity measurements locations.

region for the HF and MF airfoil in Fig. 15. The results from the dynamic Smagorinsky model accurately predicts the velocity deficit and dip location for both the angles of attack $\alpha = 0°$ and 4° at the near wake location. However, the velocity deficit is slightly overpredicted by the simulation. The width of the wake validates very well with the

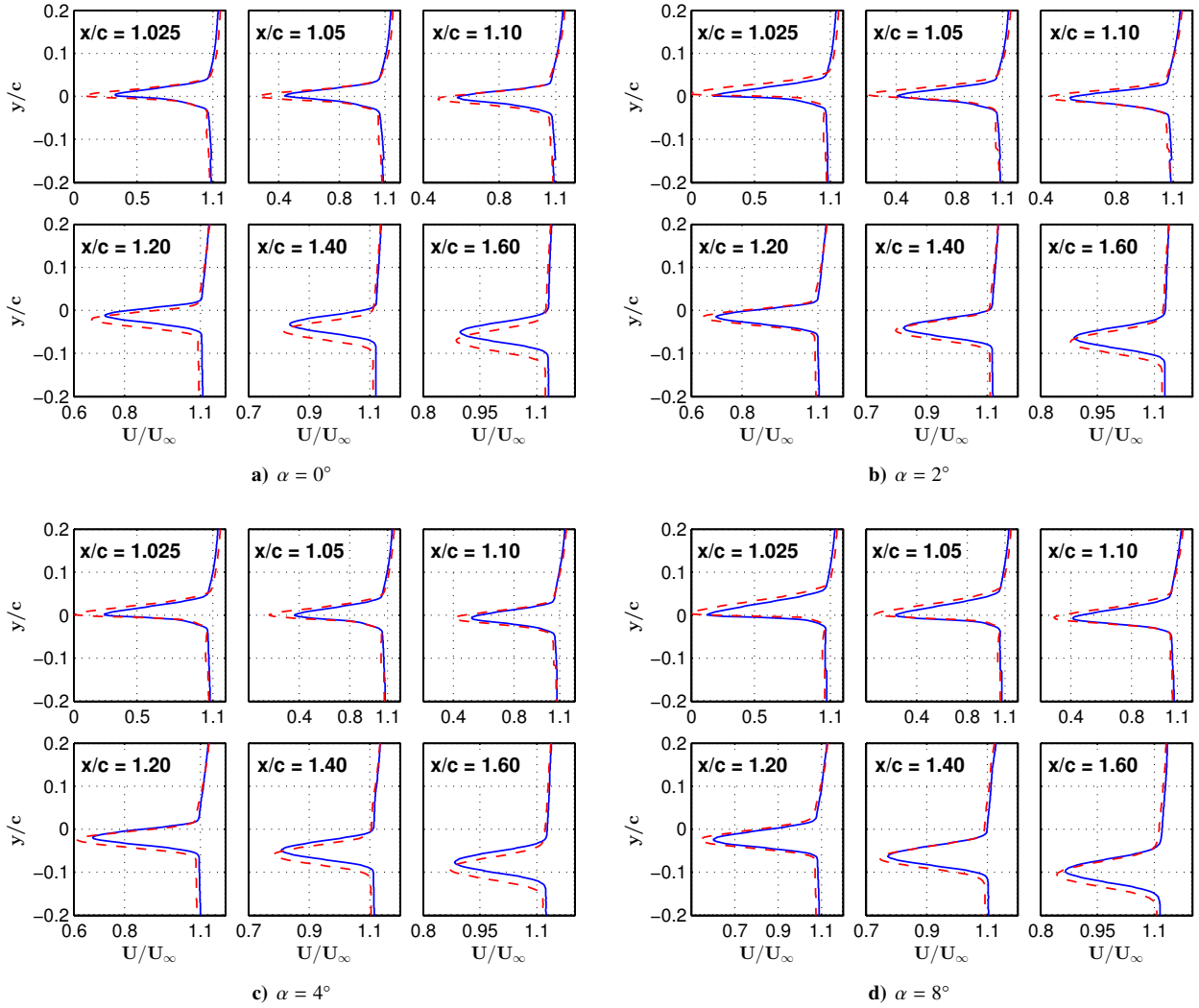

Fig. 12. Wake velocity profiles for the Hinged Flap — and Morphed Flap - - - airfoils a freestream velocity of $U_\infty = 20$ m/s ($Re_c = 2.6\times10^5$).

experimental measurements.

1. Pressure distribution

The results of the steady surface pressure distribution around both the HF and MF airfoils are presented in Figs. 16a and 16b. A sudden secondary peak in the pressure coefficient C_p at the step trip location for both the HF and MF airfoil on the suction and pressure side can be distinctly seen in the presented results. This is due to the flow acceleration over the step trip. The C_p distribution for both the airfoils reconciles with the normal trend just after $x/c < 0.25$. The suction peak of the MF airfoil at the angle of attack $\alpha = 0°$ was 11% higher relative to the HF airfoil. For the angle of attack $\alpha = 4°$ the suction peak of the MF airfoil was 8% higher relative to the HF airfoil. The results show that the change in mean camber of the flap profile of length $b = 0.3c$ at the trailing edge has an effect on the suction peak close to the airfoil leading edge. The C_p distribution over the flap at regions $x/c = 0.7 - 1.0$ for the HF and MF airfoil show significant differences between the airfoils. A third small peak in the C_p distribution on the suction side of the HF airfoil can be seen at $x/c = 0.7$. This arises due to the impingement of the flow on to the small bulge from the hinge point of the HF airfoil and can be seen for both the presented angles of attack. This third peak on the suction side is absent for the MF airfoil due to the smooth curvature of the flap profile. The results clearly show that the MF airfoil has a larger pressure difference over the entire flap region relative to the HF airfoil. This increased suction peak on the leading edge and increased pressure difference over the flap surfaces for the MF airfoil relative to the HF airfoil corresponds with the increased C_L previously seen in Sec.IV.A.

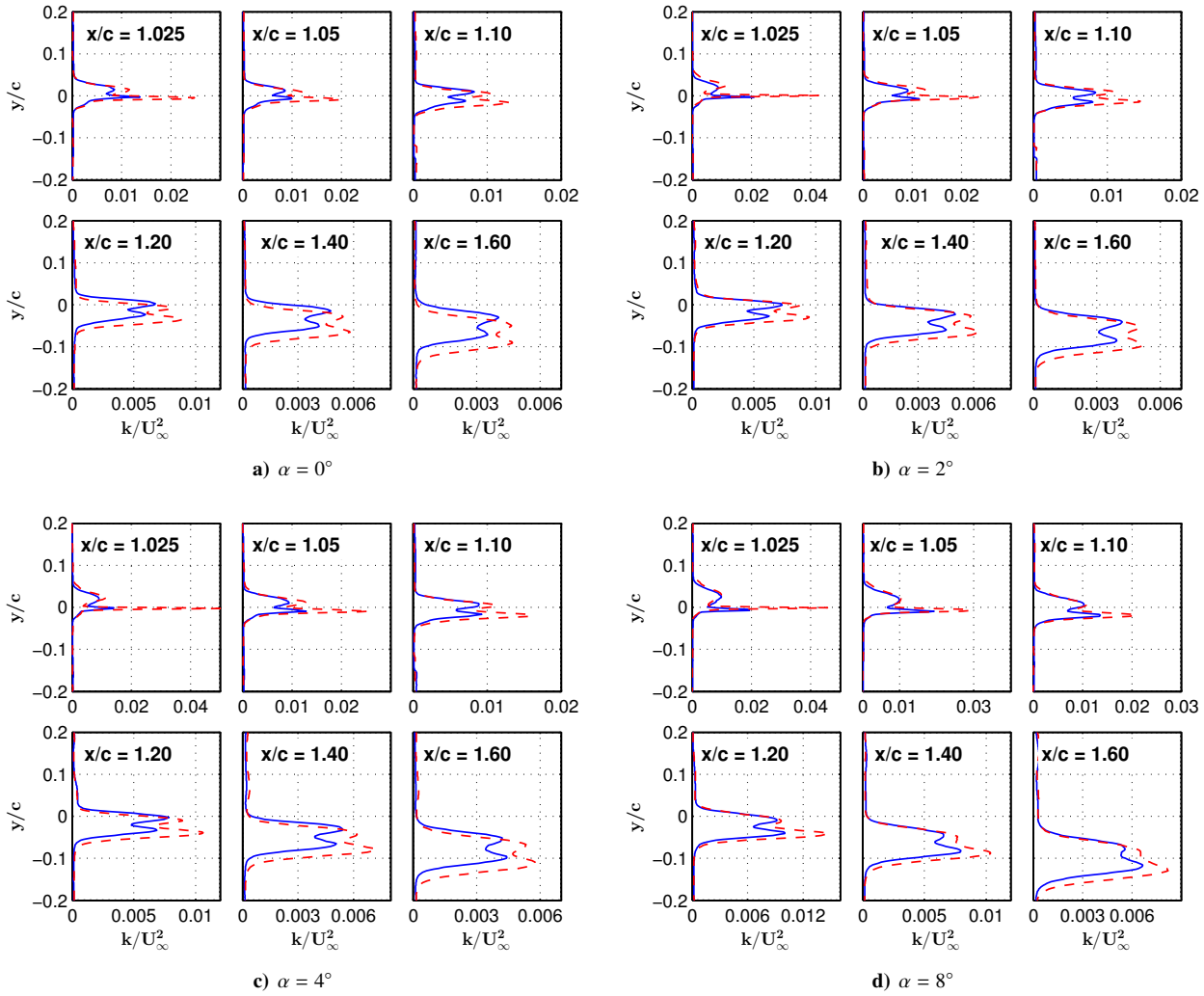

Fig. 13. Wake turbulent kinetic energy profiles for the Hinged Flap — and Morphed Flap - - - airfoils at a freestream velocity of $U_\infty = 20$ m/s ($Re_c = 2.6 \times 10^5$).

The non-dimensional pressure root mean squared over the airfoil surface is presented in Figs. 16c and 16d. The unsteady pressure distribution over the flap surface provides some insight into airfoil trailing edge noise. The results show increased fluctuations on the suction side of the HF airfoil at the hinge point location $x/c = 0.7$ but the surface pressure fluctuations subside after location $x/c \approx 0.85$. For the MF airfoil, the highly unsteady surface pressure can be seen at region $x/c = 0.9 - 1.0$ closer to the trailing edge for both the angles of attack. The higher pressure fluctuations closer to the trailing edge of the MF airfoil would potentially lead to higher noise production compared to the HF airfoil.

2. *Wake Flow Structure*

The flow field over the airfoil and in the wake region are visualized using iso-surfaces of Q-Criterion and are presented in Fig. 17. The results are presented with contours of vorticity magnitude and iso-surfaces of Q-criterion of $Q = 1 \times 10^6 s^{-2}$. The results show that the simple step-trip was sufficient to make the flow turbulent over the airfoil. The green-colored iso-surfaces of Q-Criterion indicate flow separated regions. The separated regions can be seen right behind the step-trip $x/c = 0.1$ and also right after the flap hinge point for the HF airfoil and close to the trailing edge for the MF airfoil.

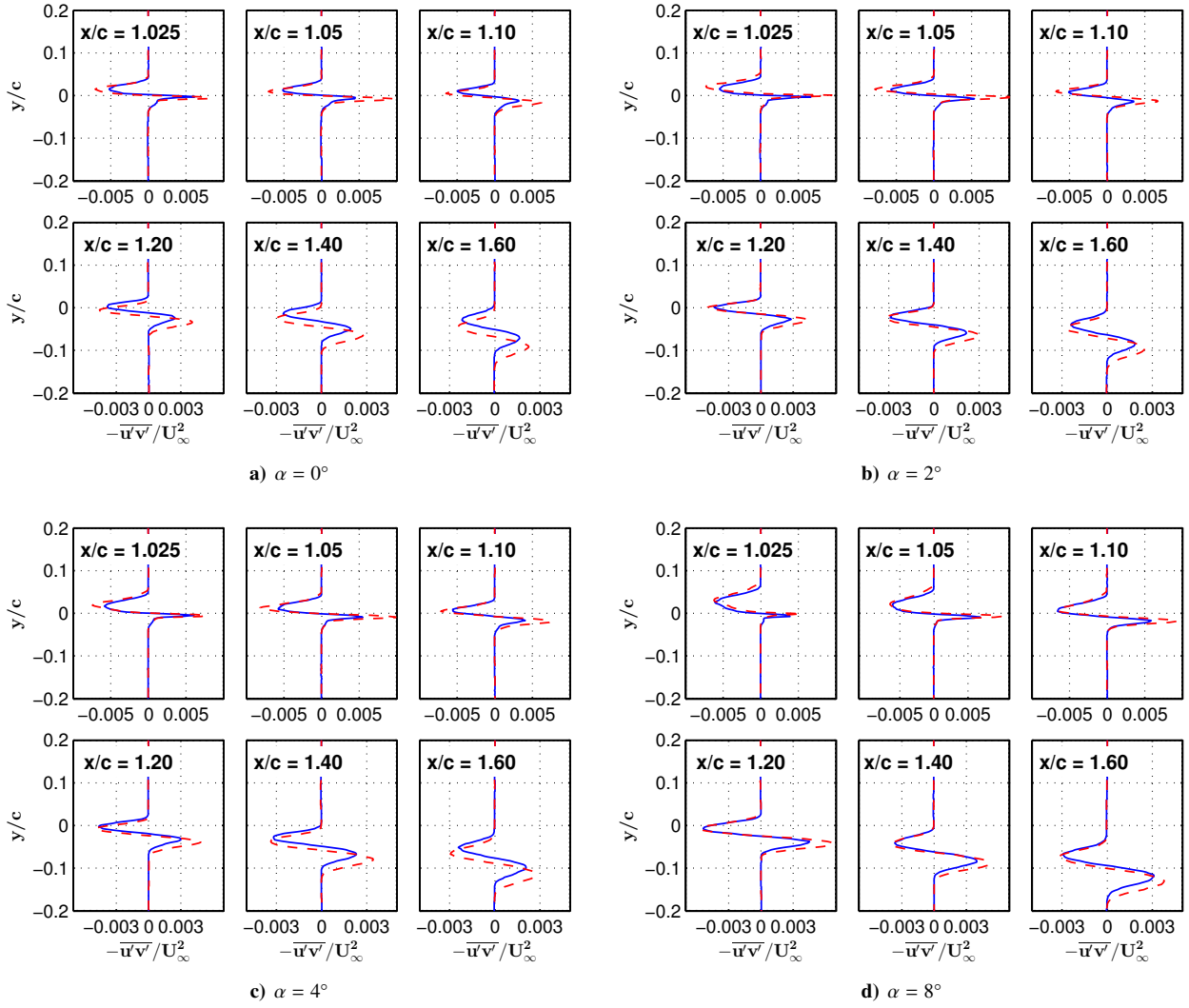

Fig. 14. Reynolds shear stress components for the Hinged Flap — and Morphed Flap - - - airfoils at a freestream velocity of $U_\infty = 20$ m/s ($Re_c = 2.6 \times 10^5$).

3. *Boundary Layer Measurements*

The non-dimensional boundary layer velocity profiles can show the separation of the flow over the flap surfaces. The boundary layer results from the LES are presented for angles of attack $\alpha = 0°$ and $4°$ in Figs. 22a and 22b, respectively. The results for the angle of attack $\alpha = 0°$ and $4°$, at streamwise location $x/c = 0.65$, before the flap hinge point show that the difference between the HF (solid line) and MF (dashed line) airfoil is insignificant. At the streamwise location, $x/c = 0.75$, the flow appears to be still attached to the surface for both the HF and MF airfoil with HF airfoil having increased velocity deficit. At further downstream locations, $x/c = 0.85$ and 0.95, the sudden decrease in the velocity gradient ($\delta U/\delta y$) for the HF airfoil determines the boundary layer separation. For the MF airfoil, the boundary layer separation can be seen only at near the trailing edge at $x/c = 0.95$. These results correspond to flow separation previously seen in the experimental results of surface flow visualization and PIV measurements in Figs. 6 and 7. The same trend was also observed in the C_p measurements in Fig. 16, where the increased fluctuations denoted the separation points.

4. *Wall Pressure Spectra*

The power spectral density Φ_{pp} of the surface pressure on the suction side for the HF and MF airfoils are presented in Fig. 19. The results in the left column are presented for angles of attack $\alpha = 0°$ and the right column are presented

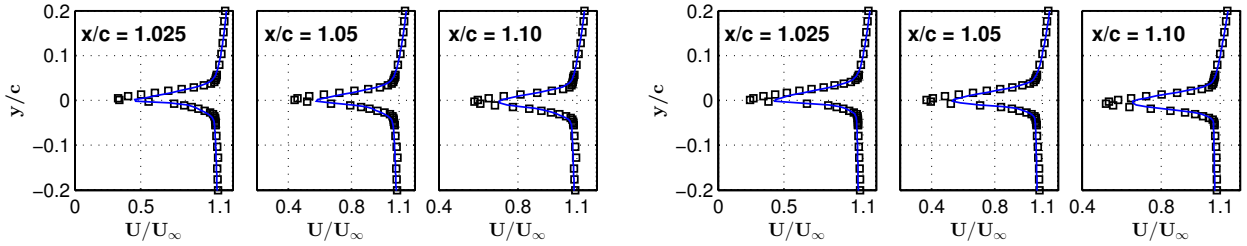

a) Hinged Flap, $\alpha = 0°$; LES —, Exp □

b) Hinged Flap, $\alpha = 4°$; LES —, Exp □

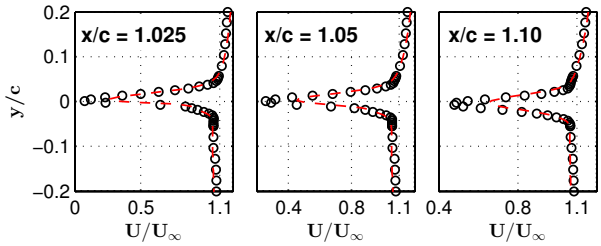

c) Morphed Flap, $\alpha = 0°$; LES - - -, Exp ○

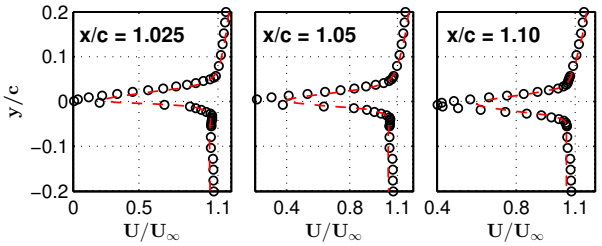

d) Morphed Flap, $\alpha = 4°$; LES - - -, Exp ○

Fig. 15. Wake velocity profiles for the Experimental measurements and LES are compared for a freestream velocity of $U_\infty = 20$ m/s ($Re_c = 2.5 \times 10^5$).

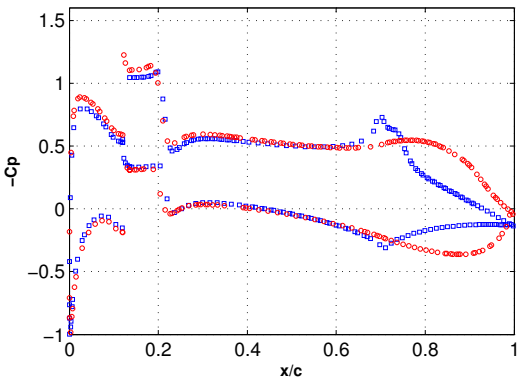

a) Pressure Coefficient, $\alpha = 0°$

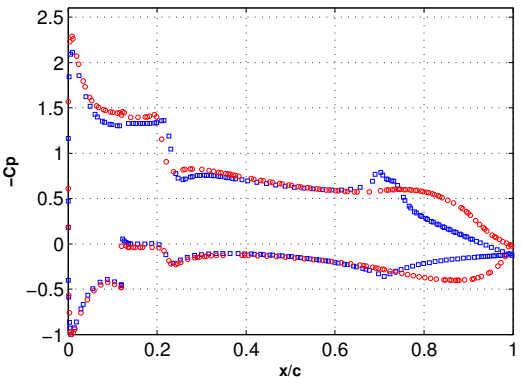

b) Pressure Coefficient, $\alpha = 4°$

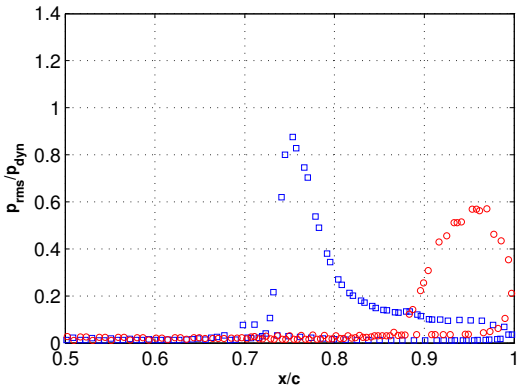

c) Pressure root mean squared, $\alpha = 0°$

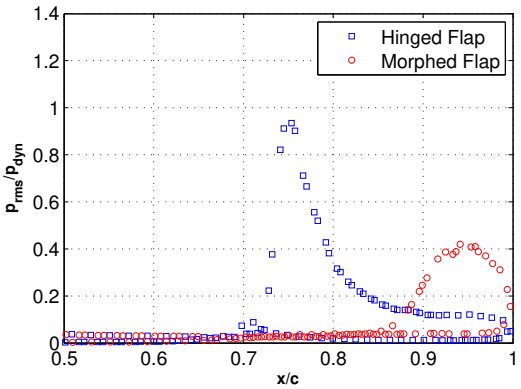

d) Pressure root mean squared, $\alpha = 4°$

Fig. 16. Pressure coefficient and pressure root mean squared over the airfoil surface for Hinged Flap and Morphed Flap airfoils at angles of attack $\alpha = 0°$ and $4°$.

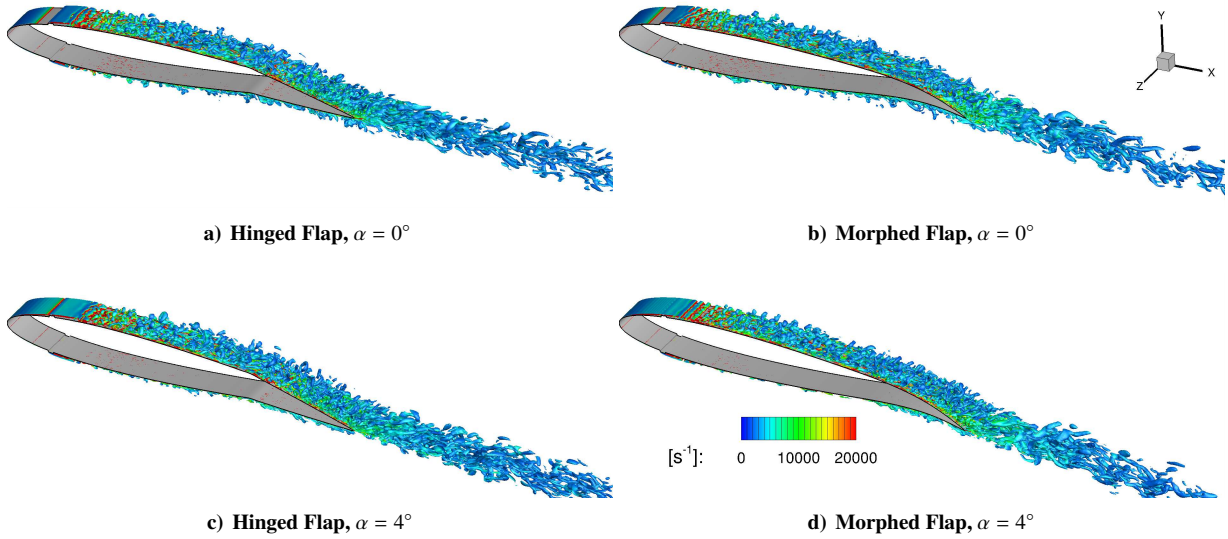

a) Hinged Flap, $\alpha = 0°$ **b) Morphed Flap, $\alpha = 0°$**

c) Hinged Flap, $\alpha = 4°$ **d) Morphed Flap, $\alpha = 4°$**

Fig. 17. Iso-surfaces of Q-criterion of $Q = 1 \times 10^6 s^{-2}$ for Hinged Flap and Morphed Flap airfoil with contours of vorticity magnitude for a freestream velocity of $U_\infty = 20$ m/s ($Re_c = 2.6 \times 10^5$).

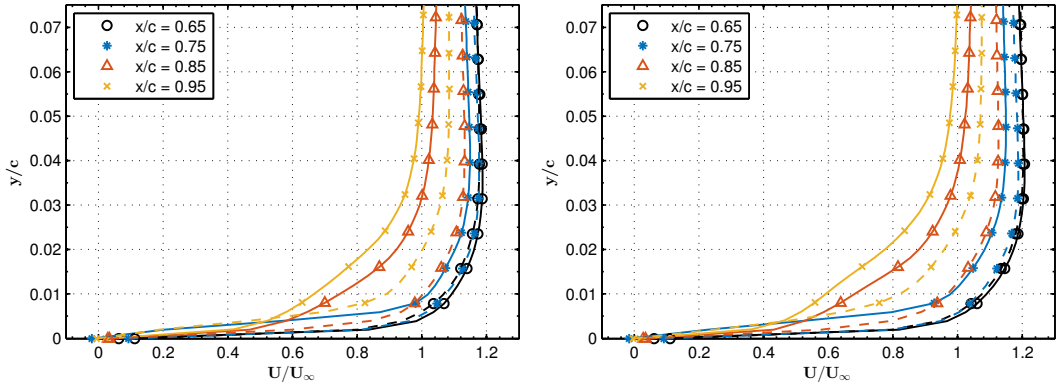

a) $\alpha = 0°$ **b) $\alpha = 4°$**

Fig. 18. Boundary layer velocity profiles on the suction side at various streamwise locations of the Hinged Flap (solid line) and Morphed Flap (dashed line) airfoils at angles of attack $\alpha = 0°$ and $\alpha = 4°$ for a freestream velocity of $U_\infty = 20$ m/s ($Re_c = 2.6 \times 10^5$).

for 4°. The results are presented at mid-span for three important streamwise locations, $x/c = 0.75$ right after the flap hinge, $x/c = 0.85$ and $x/c = 0.95$ close to the trailing edge. The wall-pressure spectra at the selected locations are important for far-field noise prediction as they are the input parameters for Curle's analogy used in this study. For both the presented angles of attack $\alpha = 0°$ and 4°, at $x/c = 0.75$ the results show the spectra is up to 20 dB higher for the HF airfoil over the entire presented frequency range (100 Hz to 10 kHz) relative to the MF airfoil. This corresponds with the increased p_{rms} seen at location $x/c = 0.75$ in Fig. 16. This broadband behavior is expected due to the fully turbulent flow over both the airfoils. The wall-pressure spectra results for both the airfoils presented in Fig. 19 at $x/c = 0.85$ show that the spectra are up to 5 dB higher for the HF airfoil at low to medium frequency range ($f \leq 4$ kHz). At further downstream locations close to the trailing edge $x/c = 0.95$, the MF airfoil has up 10 dB higher spectral levels at low to medium frequency range ($f \leq 2$ kHz) relative to the HF airfoil. This also corresponds with the higher unsteady surface pressure and separated surface flow close to the trailing edge seen earlier in the p_{rms} results (Fig. 16) and surface flow visualization results (Fig. 6).

The spanwise coherence function $\gamma^2_{p_i p_j}$ based on the fluctuating surface pressure are calculated using the Eq. 1, where N is the number of transducers. The iso- coherence contours as a function of frequency and spanwise separation for the suction side are presented in Fig. 20. The results clearly show that the MF airfoil for both the angles of attack

$\alpha = 0°$ and $4°$ at location $x/c = 0.95$ has increased the coherence of the flow structures for frequencies below 3 kHz relative to the MF airfoil. The surface pressure coherence on the spanwise direction on the suction side at location $x/c = 0.95$ is presented in Fig. 21. The coherence drops considerably for all frequencies except for MF airfoil at $kc = 1$ ($f = 273$ Hz). Therefore, the present computational domain is sufficient enough for calculation the airfoil noise over a wide frequency range.

$$\gamma^2_{p_i p_j}(f) = \frac{|\, G_{p_i p_j}(f)\,|^2}{|\, G_{p_i p_i}(f)\,||\, G_{p_j p_j}(f)\,|} \quad \text{for } p_i = 1 \text{ and } p_j = 1, 2, 3, ..., \text{N}. \tag{1}$$

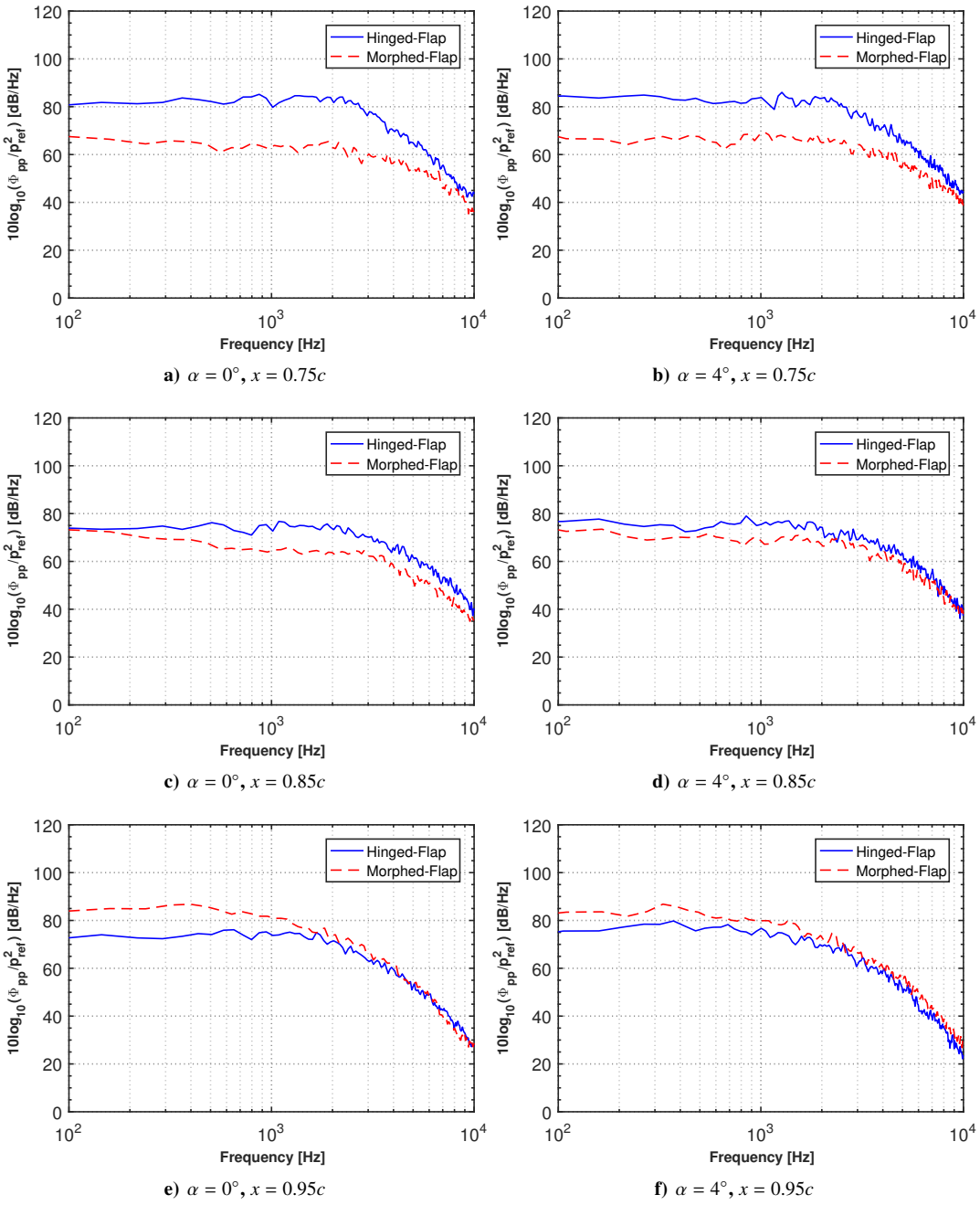

a) $\alpha = 0°$, $x = 0.75c$ **b)** $\alpha = 4°$, $x = 0.75c$

c) $\alpha = 0°$, $x = 0.85c$ **d)** $\alpha = 4°$, $x = 0.85c$

e) $\alpha = 0°$, $x = 0.95c$ **f)** $\alpha = 4°$, $x = 0.95c$

Fig. 19. Suction side wall-pressure spectra with reference to 2×10^5 Pa, at different streamwise locations for Hinged Flap and Morphed Flap airfoils at angles of attack $\alpha = 0°$ and $4°$ for a freestream velocity of $U_\infty = 20$ m/s ($Re_c = 2.6 \times 10^5$).

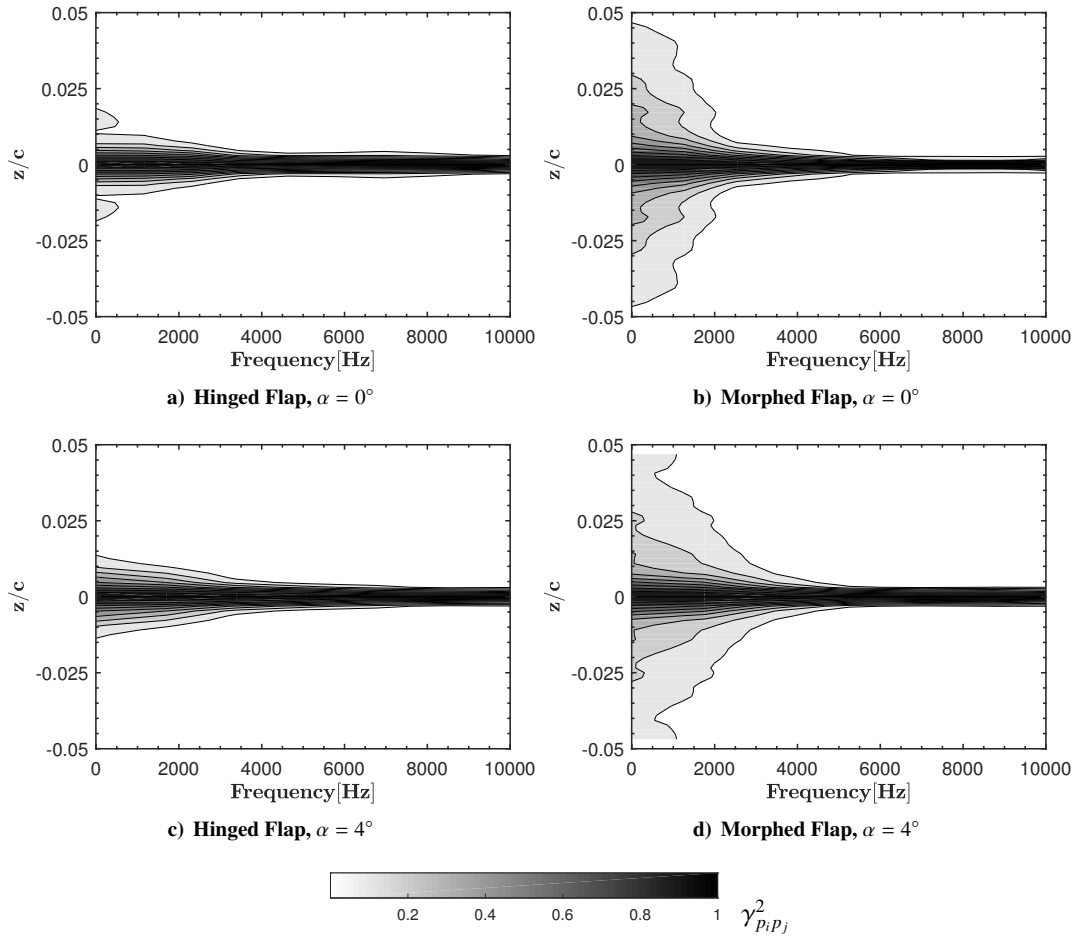

a) Hinged Flap, $\alpha = 0°$ **b) Morphed Flap,** $\alpha = 0°$

c) Hinged Flap, $\alpha = 4°$ **d) Morphed Flap,** $\alpha = 4°$

Fig. 20. Spanwise coherence of the surface pressure, at the location $x = 0.95c$ **for Hinged Flap and Morphed Flap airfoils at angles of attack** $\alpha = 0°$ **and** $4°$ **for a freestream velocity of** $U_\infty = 20$ **m/s (**$Re_c = 2.6 \times 10^5$**).**

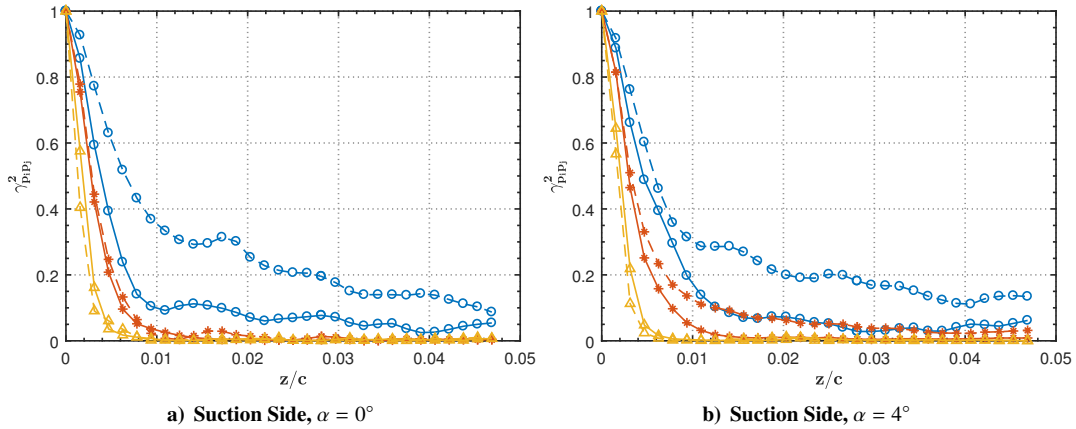

a) Suction Side, $\alpha = 0°$ **b) Suction Side,** $\alpha = 4°$

Fig. 21. Spanwise coherence of the surface pressure at the location $x = 0.95c$ **for Hinged Flap (solid line) and Morphed Flap (dashed line) airfoils at angles of attack** $\alpha = 0°$ **and** $4°$ **for** $kc = 1$ **(circles)** $kc = 10$ **(asterisk) and** $kc = 20$ **(triangle).**

5. *Far-field Noise*

Trailing-edge noise computations were performed using Curle's acoustic analogy [34]. The source terms for the Curle's analogy are the surface pressure fluctuations acquired at every time step of the LES simulations for the last 10 FTT. The far-field noise calculations were made at 1.2 m above the trailing edge of both the airfoils and the sound

pressure level results in reference to P_{ref} are presented in Fig. 22. The results at the angle of attack $\alpha = 0°$ show that the sound level for the MF airfoil is up to 10 dB higher than the HF airfoil below $f < 1$ kHz. The noise levels for frequency range higher than $f > 1$ kHz the difference between the HF and MF airfoil are insignificant. For $\alpha = 4°$, the broadband noise is ≈ 5 dB higher for the MF airfoil compared to the HF airfoil below $f < 800$ Hz. This corresponds to the increased spanwise coherence seen earlier in Figs. 20 and 21.

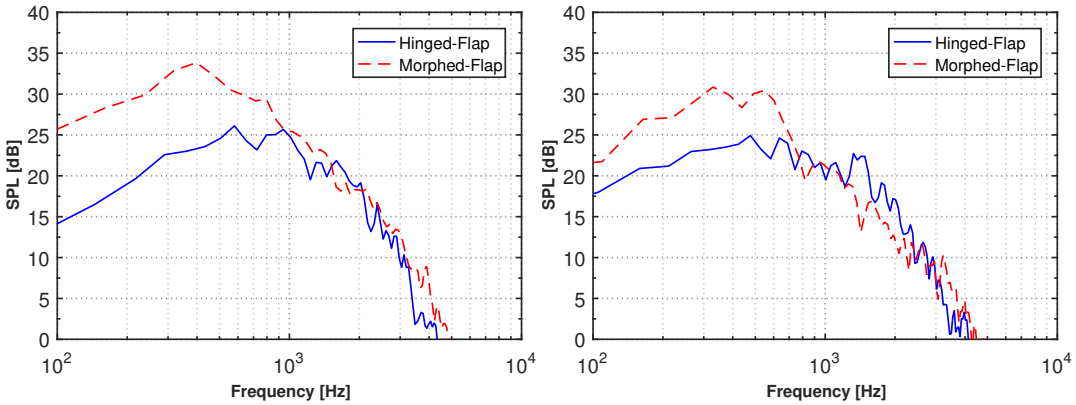

a) $\alpha = 0°$ **b)** $\alpha = 4°$

Fig. 22. Acoustic prediction using Curle's analogy, sound pressure level in dB reference to 2×10^5 Pa, at the location 1.2 m above the trailing edge for Hinged Flap and Morphed Flap 4 airfoils at angles of attack $\alpha = 0°$ and $4°$ for a freestream velocity of $U_\infty = 20$ m/s ($Re_c = 2.6 \times 10^5$).

V. Conclusion

The aerodynamic and aeroacoustic performance of NACA 0012 airfoil fitted with Hinged- and Morphed Flap were investigated using experimental and numerical techniques. The airfoil was tested for a flow velocity of $U_\infty = 20$ m/s, corresponding to a chord-based $Re_c = 2.6 \times 10^5$. Surface flow visualization, aerodynamic lift and drag measurements and flow measurements using PIV technique were carried out to better understand the flow characteristics of the HF and MF airfoils. The lift and drag measurements showed an increase of up to $C_{L,max} = 14\%$ for the MF airfoil relative to the HF airfoil. The C_L/C_D performance at low angles of attack showed an improvement of up to 6% for MF airfoil. Surface flow visualization results showed delayed separation over the flap for the MF airfoil compared to the HF airfoil. The mean velocity results showed increased wake deficit for the MF airfoil compared to the HF airfoil at the near-wake locations $x/c = 1.025, 1.05$ and 1.10 along with increased flow turning angle at far-wake locations $x/c = 1.20, 1.40$ and 1.60. The results of the turbulent kinetic energy at the airfoil wake was up to 50% higher for the MF airfoil relative to the HF airfoil for all the presented angles of attack. The turbulent kinetic energy displayed a characteristic double peak behavior, which is also the major content of the streamwise normal Reynolds stress component ($\overline{u'u'}$). The peak values of the $\overline{u'u'}$ can be observed close to the trailing edge point. The Reynolds shear stress component ($\overline{u'v'}$) for the MF airfoil is larger than that of the HF airfoil at the near-wake locations $x/c = 1.025$, $x/c = 1.05$ and $x/c = 1.10$ for all the presented angles of attack. The MF airfoil shows improved C_L/C_D performance compared to the HF airfoil. The increased turning angle for the MF airfoil results in the increased lift and the longer region of attached flow near the trailing edge results in the reduction of form drag producing improved C_L/C_D for the MF airfoil. The surface pressure root mean squared results from the LES showed increased fluctuations for the HF airfoil right after the flap hinge point at $x/c = 0.75$ but the fluctuations move further downstream closer to the trailing edge for the MF airfoil. The wall pressure spectra at close to the trailing edge show increased energy for the MF airfoil. The far-field noise measurements were computed using Curle's acoustic analogy and the results show increased noise for the MF airfoil and this can be related to the increased pressure fluctuations that are close to the trailing edge for the MF airfoil.

References

[1] Lockard, D.P., and Lilley, G.M., *The Airframe Noise Reduction Challenge*, NASA-TM-2004-213013, 2004.

[2] Wagner, S., Bareriss, R., and Guidati, G. *Wind Turbine Noise*, Springer: Berlin, 1996, pp: 67-92.

[3] Liu, X., Kamliya Jawahar, H., Azarpeyvand, M., and Theunissen, R. "Aerodynamic Performance and Wake Development of Airfoils with Serrated trailing edges", AIAA Journal, Vol. 55, No. 11 (2017), pp: 3669-3680.

[4] Lyu, B., Azarpeyvand, M., and Sinayoko, S., "Prediction of Noise from Serrated trailing edges", *Journal of Fluid Mechanics*, Vol. 793, pp: 556-588, 2016.

[5] Liu, H.R., Azarpeyvand, M., Wei, J.J., and Qu, Z.G., "Tandem Cylinder Aerodynamic Sound Control Using Porous Coating", *Journal of Sound and Vibration*, Vol. 334, pp: 190-201, 2015.

[6] Showkat Ali, S. A., Liu, X., and Azarpeyvand, M., "Bluff Body Flow and Noise Control Using Porous Media", AIAA 2016-2754, 2016.

[7] Showkat Ali, S. A., Szoke, M., Azarpeyvand, M., and Ilario, C., "Trailing edge Bluntness Flow and Noise Control Using Porous Treatments", AIAA 2016-2832, 2016.

[8] Showkat Ali, S. A., Szoke, M., Azarpeyvand, M., and Ilario, C., "Experimental Study of Porous Treatment for Aerodynamic and Aeroacoustic Purposes", AIAA 2017-3358, 2017.

[9] Kamliya Jawahar, H., Azarpeyvand, M., and Carlos R.Ilario. "Experimental Investigation of Flow Around Three-Element High-Lift Airfoil with Morphing Fillers", AIAA 2017-3364, 2017.

[10] Ai, Q., Kamliya Jawahar, H., and Azarpeyvand, M., "Experimental Investigation of Aerodynamic Performance of Airfoils Fitted with Morphing trailing edges", AIAA 2016-1563, 2016.

[11] Kamliya Jawahar, H., Ai, Q., and Azarpeyvand, M., "Experimental and Numerical Investigation of Aerodynamic Performance of Airfoils Fitted with Morphing trailing edges", AIAA 2017-3371, 2017.

[12] Kamliya Jawahar, H., Ai, Q., and Azarpeyvand, M., "Experimental and Numerical Investigation of Aerodynamic Performance of Airfoils with Morphed trailing edges", Renewable Energy, Vol. 127, (2018), pp: 355-367.

[13] Gad-el-Hak, M. *Flow Control: Passive, Active, and Reactive Flow Management*; Cambridge University Press: New York, 2006.

[14] Sanders, B., Eastep, F.F., and Froster, E. "Aerodynamic and Aeroelastic Characteristics of Wings with Conformal Control Surfaces for Morphing Aircraft", *Journal of Aircraft*, Vol. 40, No. 1, pp: 94-99, January 2003.

[15] Daynes, S., and Weaver, M.P., "A Morphing trailing edge Device for a Wind Turbine", *Journal of Intelligent Material Systems and Structures*, Vol. 23, No. 6, pp: 691-701, March 2012.

[16] Wolff, T., Ernst, B., and Seume, J.R., "Aerodynamic Behaviour of an Airfoil with Morphing trailing edge for Wind Turbine Application", *The Science of Making Torque from Wind 2014*, June 2014.

[17] Campanile, L.F., and Anders, S., "Aerodynamic and Aeroelastic Amplification in Adaptive Belt-rib Airfoils", *Aerospace Science and Technology*, Vol. 9, pp:55-63, September 2004.

[18] Yokozeki, T., Sugiura,A., and Hirano,Y. "Development of Variable Camber Morphing Airfoil Using Corrugated Structure", *Journal of Aircraft*, Vol. 51, No. 3, pp:1023-1029, May 2014.

[19] Ai, Q., Azarpeyvand, M., Lachenal, X., and Weaver, P., "Aerodynamic and Aeroacoustic Performance of Airfoils Using Morphing Structures", *Wind Energy*, Vol. 19, No. 7, pp:1325-1339, July 2016.

[20] Ai, Q., Azarpeyvand, M., Lachenal, X., and Weaver, P., "Airfoil Noise Reduction Using Morphing trailing edge", *The 21st International Congress on Sound and Vibration*, Beijing, China., July 2014.

[21] Barrett R.V., "Design and Performance of a New Low Turbulence Wind Tunnel at Bristol University", *The Aeronautical Journal*, Vol. 88, No. 873, pp: 86-90, March 1984.

[22] Lyon, C. A., Selig, M. S., and Broeren, A. P., "Boundary Layer Trips on Airfoils at Low Reynolds Numbers ", AIAA 97-0511 , 1997.

[23] Lyon, C. A., Broeren, A. P., Golalarathnam, A., and Selig, M. S., *Chapter 6: Boundary Layer Trips, Summary of Low-Speed Airfoil Data Volume 3*, SoarTech Publications: Virginia, 1997, pp:331-341.

[24] Serdar Genc, M., Karasu, I., and Hakan Ackel, H., "An Experimental Study on Aerodynamics of NACA2415 Aerofoil at Low Re Numbers", *Experimental Thermal and Fluid Science*, Vol. 39, pp:252-264, 2012.

[25] Perrens, D.F., "Flow Visualisation in Low Speed Wind Tunnels", *Physics in Education*, Vol. 5, pp:262-265, 1970.

[26] Lilly D. K., "A Proposed Modification of the Germano Subgrid-Scale Closure Method.", *Physics of Fluids*, Vol. 4, pp: 633-635, 1992.

[27] Mellen C. P., Frograve J., hlich., and Rodi W., "Lessons from LESFOIL Project on Large-Eddy Simulation of Flow Around an Airfoil", *AIAA Journal*, Vol. 41, No. 4, pp: 573-581, 2003.

[28] Wolf W. R., Azevedo J. L., and Lele S. K., "Convective Effects and the Role of Quadrupole Sources for Aerofoil Aeroacoustics", *Journal of Fluid Mechanics*, Vol. 708, pp: 502-538, 2012.

[29] Winkler J., Moreau S., and Carolus T., "Airfoil trailing edge Blowing: Broadband Noise Prediction from Large-Eddy Simulation", *AIAA Journal*, Vol. 50, No. 2, pp: 294-303, 2012.

[30] Kamliya Jawahar H., Lin Y., and Savill M., "Large Eddy Simulation of Airfoil Self-noise using OpenFOAM", *Aircraft Engineering and Aerospace Technology*, Vol. 90, No.1, pp: 126-133, 2018.

[31] Carl J. Wenzinger, "Wind-Tunnel Investigation of Ordinary and Split Flaps on Airfoils of Different Profile, *NACA-Report-No.544*, 1937.

[32] Neeuhart D. H., Pendergraft O. C., "A water tunnel study of Gurney flaps, *NASA TM 4041*, 1988.

[33] Jang C. S., Ross J. C., and Cummings R. M., "Computational evaluation of an airfoil with a Gurney flap", AIAA 92-2708, 2016.

[34] Curle, N. "The Influence of Solid Boundaries upon Aerodynamic Sound." *Proceedings of the Royal Society of London* Vol. 231. No. 1187, pp: 505514, 1955.